

# Hyperconjugation-Controlled Molecular Conformation Weakens Lithium-Ion Solvation and Stabilizes Lithium Metal Anode

Yuelang Chen<sup>†1,2</sup>, Sheng-Lun Liao<sup>†1</sup>, Huixin Gong<sup>1</sup>, Zewen Zhang<sup>3</sup>, Zhuojun Huang<sup>3</sup>, Sang Cheol Kim<sup>3</sup>, Elizabeth Zhang<sup>1,3</sup>, Hao Lyu<sup>1</sup>, Weilai Yu<sup>1</sup>, Yangju Lin<sup>1</sup>, Philaphon Sayavong<sup>2,3</sup>, Yi Cui\*<sup>3,4,5</sup>, Jian Qin\*<sup>1</sup>, Zhenan Bao\*<sup>1</sup>

<sup>1</sup>Department of Chemical Engineering, Stanford University, Stanford, CA, USA.

<sup>2</sup>Department of Chemistry, Stanford University, Stanford, CA, USA.

<sup>3</sup>Department of Materials Science and Engineering, Stanford University, Stanford, CA, USA.

<sup>4</sup>Department of Energy Science and Engineering, Stanford University, Stanford, CA, USA.

<sup>5</sup>Stanford Institute for Materials and Energy Sciences, SLAC National Accelerator Laboratory, Menlo Park, CA, USA.

<sup>†</sup>Y.Chen and S.L. contributed equally to this work.

\*Correspondence and request for materials should be addressed to Z.B. (email: [zbao@stanford.edu](mailto:zbao@stanford.edu)), Y. Cui (email: [yicui@stanford.edu](mailto:yicui@stanford.edu)), or J.Q. (email: [jianq@stanford.edu](mailto:jianq@stanford.edu))

## Abstract

Tuning the solvation structure of lithium ions via electrolyte engineering has proven effective for lithium metal (Li) anode. Further advancement that bypasses the trial-and-error practice relies on the establishment of molecular design principles. Expanding the scope of our previous work on solvent fluorination, we report here an alternative design principle for non-fluorinated solvents, which

potentially have reduced cost, environmental impact, and toxicity. By studying non-fluorinated ethers systematically, we found that the short-chain acetals favor the [gauche, gauche] molecular conformation due to hyperconjugation, which leads to weakened monodentate coordination with Li<sup>+</sup>. The dimethoxymethane electrolyte showed fast activation to >99% Coulombic efficiency (CE) and high ionic conductivity of 8.03 mS cm<sup>-1</sup>. The electrolyte performance was demonstrated in anode-free Cu | LFP pouch cells at current densities up to 4 mA cm<sup>-2</sup> (70 to 100 cycles) and thin-Li | high-loading-LFP coin cells (200-300 cycles). Overall, we demonstrated and rationalized the improvement in Li metal cyclability by the acetal structure compared to ethylene glycol ethers. We expect further improvement in performance by tuning the acetal structure.

## Introduction

Lithium-metal (Li) electrode has attracted enormous research interest.<sup>1</sup> However, its high reactivity and large volume change pose significant challenges to battery stability.<sup>2,3</sup> Electrolyte design is an effective strategy to overcome the instability.<sup>4</sup> In recent years, numerous advanced electrolytes have enabled Li | Cu half-cell Coulombic efficiency (CE) of >99% with the desired chunky Li deposition morphology.<sup>5-22</sup> The combination of LiFSI with rationally designed solvent(s) is among the most successful strategies.<sup>11,23</sup> By controlling the solvation structure of Li<sup>+</sup>, FSI<sup>-</sup>-derived inorganic-rich SEI becomes more dominant<sup>4</sup>, which swells less<sup>24</sup> and dissolves less<sup>25</sup> in the electrolyte and remains mechanically robust and chemically passivating. Following this design, our groups<sup>11,15,26</sup> and others<sup>17,18,27,28</sup> developed several solvents that enabled quick and effective passivation of Li electrode, where the initial CE reached >99% within 5 cycles<sup>11,15</sup> and stable CE reached 99.9% after 100 cycles in Li | Cu half cells<sup>11</sup>.

Despite these progresses, the understanding of molecular design principles is still limited. Solvent fluorination has been proven effective to tune the Lewis basicity of solvents, and thereby their solvation

ability.<sup>11,15,29,30,31,32</sup> However, fluorinated organic molecules face potential issues with cost, environmental concerns, and toxicity. Therefore, it is of great interest to develop additional molecular design principles. We recently reported steric hindrance as an alternative, effective design strategy.<sup>26</sup> However, given the vast tunability of organic molecules, the molecular design space remains largely unexplored.

Herein, we report a new molecular design strategy, where we use solvent molecular conformation to tune Li<sup>+</sup> solvation structure and electrolyte reactivity. Ethylene glycol ethers have a relatively flexible dihedral angle between the two O-CH<sub>2</sub> bonds, which enables bidentate chelation with Li<sup>+</sup>. In contrast, acetals favor gauche conformation between O-CH<sub>3</sub> and O-CH<sub>2</sub> bonds due to hyperconjugation, which results in weak monodentate coordination with Li<sup>+</sup> (Figure 1a). Notably, two recent publications<sup>33,34</sup> reported the weakly solvating nature of acetal solvents, but they proposed an anti conformation for acetals.

The electrochemical performance was evaluated with 0.9 M and 3 M lithium bis(fluorosulfonyl)imide (LiFSI), representative of standard and high concentration electrolytes. Both dimethoxymethane (DMM) and diethoxymethane (DEM) as examples of acetals showed faster stabilization of Li CE compared to 3 M LiFSI / DEE<sup>26</sup>. Impressively, the DMM electrolytes reached >99% CE within 3 to 5 cycles at 0.5 mA cm<sup>-2</sup> and 1 mAh cm<sup>-2</sup> in Li|Cu half cells, which is comparable to the best fluorinated ethers<sup>11,15</sup>. In addition, the high ionic conductivity and transport number of 3 M LiFSI / DMM enabled low overpotentials of 55 mV at 6 mA cm<sup>-2</sup> and 85 mV at 10 mA cm<sup>-2</sup> in Li|Li cells. The overall benefits of fast CE activation, high CE, and good ion transport were seen in thin-Li|LFP coin cells and anode-free Cu|LFP pouch cells.

## Results and discussions

**Molecular Structures and design principle.** Ethylene glycol ethers, such as 1,2-dimethoxyethane<sup>16</sup> (DME) and 1,2-diethoxyethane<sup>26</sup> (DEE), are among the most commonly used solvents for Li metal anode due to their reductive stability. Despite relatively low permittivity<sup>35</sup>, these ethers exhibit good Li salt solubility through chelation effect—the bidentate ligands can form a stable five-membered ring with Li<sup>+</sup> (Figure 1a). However, the strong coordination between solvent and Li<sup>+</sup> results in fewer ion pairs or aggregates and, subsequently, disfavors the formation of anion-derived SEI.<sup>4</sup> Previously, we utilized fluorine substitution<sup>11</sup> and steric effect<sup>9</sup> to weaken the coordination ability of ethylene glycol ethers. Herein, we report a third molecular design strategy that weakens the Li<sup>+</sup>-solvent interaction by controlling the conformation of solvent molecules.

We demonstrate this strategy by studying the solvation behaviors of dimethoxymethane (DMM) and diethoxymethane (DEM). We hypothesize that acetals are weak monodentate ligands because (1) the stabilization effect from chelation is reduced due to the more strained structure from the shortened distance between two oxygens (Figure 1a) and (2) the molecular conformation due to hyperconjugation<sup>36,37,38</sup> (Figure 1b, Supplementary Discussion 1) leads to the opposite orientations of charge density on each oxygen and significantly reduces chelation with Li<sup>+</sup> (Figure 1a).

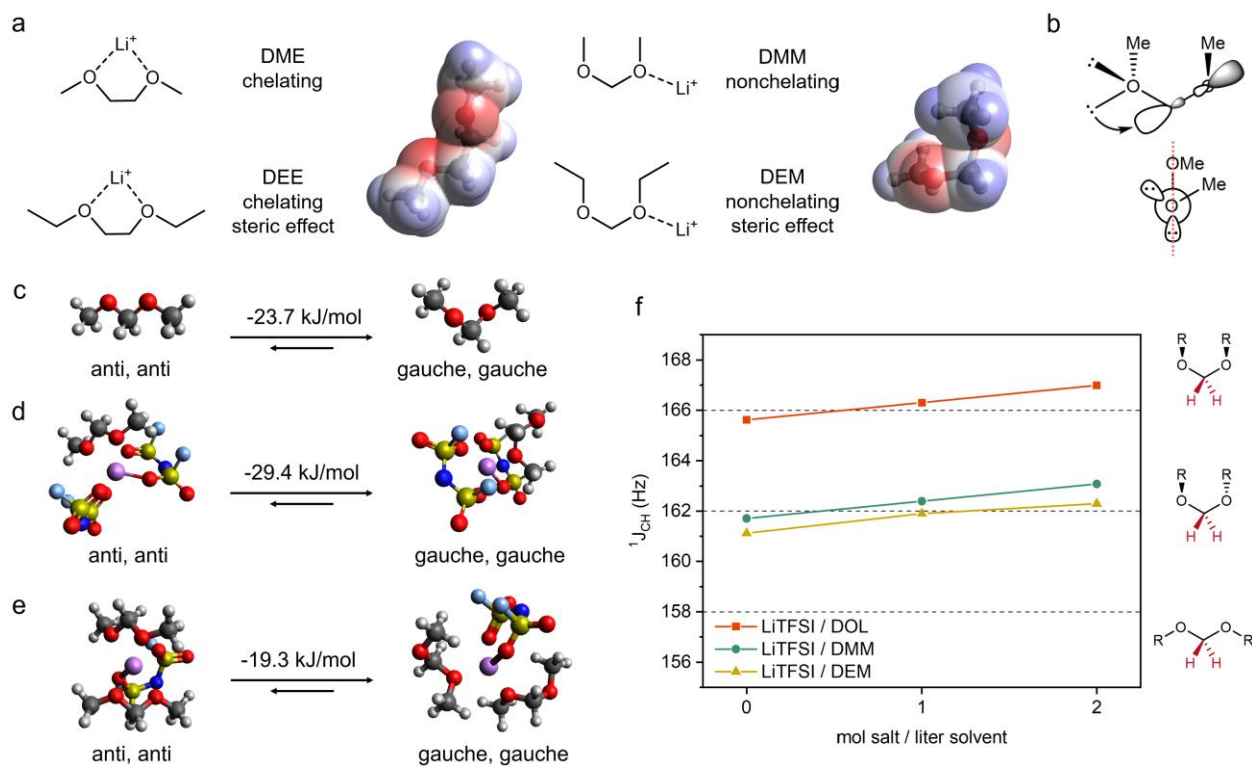


Figure 1. Solvent coordination geometry as a design strategy for LMB electrolytes. (a) The most stable coordination geometries of solvent molecules with  $\text{Li}^+$ . The electrostatic potential surfaces of DME and DMM show different orientations of negative charge density around oxygens. (b) Schematic structure of DMM showing hyperconjugation between O lone pair electrons and C-O sigma antibonding orbital, of which the orbital alignment is shown in the Newman projection. Note there are two pairs of such interactions per acetal. (c-e) DFT calculated ground state energy difference between structures containing [anti, anti] and [gauche, gauche] conformations of DMM. (c) A single DMM molecule. (d) A solvation structure of 2  $\text{FSI}^-$  and 1 DMM around  $\text{Li}^+$ . (e) A solvation structure of 1  $\text{FSI}^-$  and 2 DMM around  $\text{Li}^+$ . (f)  $^1\text{J}_{\text{CH}}$  coupling constants of anomeric  $-\text{CH}_2-$  of DOL, DMM and DEM with various concentrations of LiTFSI. The dash lines indicate the expected  $^1\text{J}_{\text{CH}}$  for each molecular geometry shown on the right.<sup>38</sup> The anomeric position is indicated in red.

Previous work confirmed the [gauche, gauche] conformation of pure DMM and DEM.<sup>37,38</sup> However, it is unclear whether Li<sup>+</sup> coordination could alter their conformation. Therefore, we used density functional theory (DFT) calculation (Supplementary Discussion 2) to determine the optimal solvent conformation within solvation shells (1 Li<sup>+</sup>, 2 FSI<sup>-</sup>, 1 DMM and 1 Li<sup>+</sup>, 1 FSI<sup>-</sup>, 2 DMM) and outside solvation shell (Figure 1c-e). These typical solvation shell compositions were selected based on previous reports on weakly solvating electrolytes<sup>11,15</sup>, and they will be confirmed in the later section. Similar to pure DMM, the solvation complexes with [gauche, gauche] DMM are more stable than those with [anti, anti] DMM by 19 to 29 kJ/mol. The optimized structures show that [anti, anti] DMM is bidentate (i.e. two oxygens per DMM coordinating to one Li<sup>+</sup>) whereas [gauche, gauche] DMM is monodentate (i.e. one oxygen per DMM coordinating to one Li<sup>+</sup>). Consistent with our rationales above, the energy gain of chelation is minimal compared to the energy penalty of breaking hyperconjugation in DMM. We expect the same behavior in DEM since the intramolecular steric strain is similar for ethyl and methyl groups in [gauche, gauche] acetals—the nonlinear geometry should be significantly more stable in DEM as well.<sup>38</sup>

The DFT results above were cross validated by 1D NMR experiments. The carbon-proton one-bond coupling constant at anomeric position ( $^1\text{J}_{\text{CH}}$ ) is dependent on conformation.<sup>39</sup> Based on literature report for acetals<sup>38</sup>,  $^1\text{J}_{\text{CH}} < 158$  Hz corresponds to [anti, anti] conformation,  $^1\text{J}_{\text{CH}} \sim 162$  Hz corresponds to [gauche, gauche] with R groups on the opposite planes, and  $^1\text{J}_{\text{CH}} > 166$  Hz corresponds to [gauche, gauche] with R groups on the same plane (Figure 1f). A cyclic acetal, 1,3-dioxolane (DOL), was used as a control since it cannot adopt [anti, anti] conformation. The  $^1\text{J}_{\text{CH}}$  values of DOL, DMM and DEM were measured with various LiTFSI concentrations. Both pure DMM and DEM have  $^1\text{J}_{\text{CH}}$  close to 162 Hz corresponding to [gauche, gauche], whereas pure DOL shows  $^1\text{J}_{\text{CH}}$  right below 166 Hz due to a puckered conformation as shown in a previous report.<sup>40</sup> As LiTFSI concentration increases, the  $^1\text{J}_{\text{CH}}$  values of DMM and DEM are around 162 Hz, corresponding to [gauche, gauche] conformation. In addition, DMM and DEM follow the same trend as DOL, which further confirms that DMM and DEM do not adopt [anti, anti] conformation.

when coordinated with Li<sup>+</sup>. The same experiment was carried out using LiFSI in DMM and DEM (Supplementary Figure S1), where the same trend was observed.

Based on DFT calculation and NMR experiment above, we conclude that both DMM and DEM remain in [gauche, gauche] conformation irrespective of whether they are coordinated with Li<sup>+</sup>. This molecular conformation prevents DMM and DEM from bidentate chelating with Li<sup>+</sup> due to the orientation of negative charge density on each oxygen as well as the distance between two oxygens. Therefore, this suggests that the solvating ability of monodentate DMM and DEM are weaker than that of bidentate DME and DEE.

**Solvation structures.** To verify our hypothesis above, the solvation structures of LiFSI in various solvents were investigated. For each solvent, 1 and 4 moles of LiFSI per liter of solvent were prepared, corresponding to standard (~0.9 M) and high (~3 M) concentration electrolytes, respectively. The molarity and molality for each electrolyte are listed in Supplementary Table S1.

We first quantify the strength of solvation by measuring the difference between the chemical potentials of Li<sup>+</sup> in sample electrolytes and a common reference electrolyte,  $\Delta\mu_{\text{Li}^+} = \mu_{\text{Li}^+}^{\text{test}} - \mu_{\text{Li}^+}^{\text{ref}}$ , using the method detailed in our previous work<sup>41</sup>. A higher  $\Delta\mu_{\text{Li}^+}$  correlates to weaker Li<sup>+</sup> solvation, and thereby stronger Li<sup>+</sup>-FSI<sup>-</sup> interactions.<sup>41,42,43</sup> We found that  $\Delta\mu_{\text{Li}^+}$  increases in the order of DME < DEE < DMM < DEM, for both 0.9 M and 3 M LiFSI (Figure 2a), confirming weaker solvation of Li<sup>+</sup> by DMM and DEM. Notably, despite being fluorine-free, DMM and DEM electrolytes show similar  $\Delta\mu_{\text{Li}^+}$  as trifluorinated and tetrafluorinated DEE electrolytes at low concentrations<sup>11</sup>, which confirms the impact of solvent coordination geometry on solvation ability.

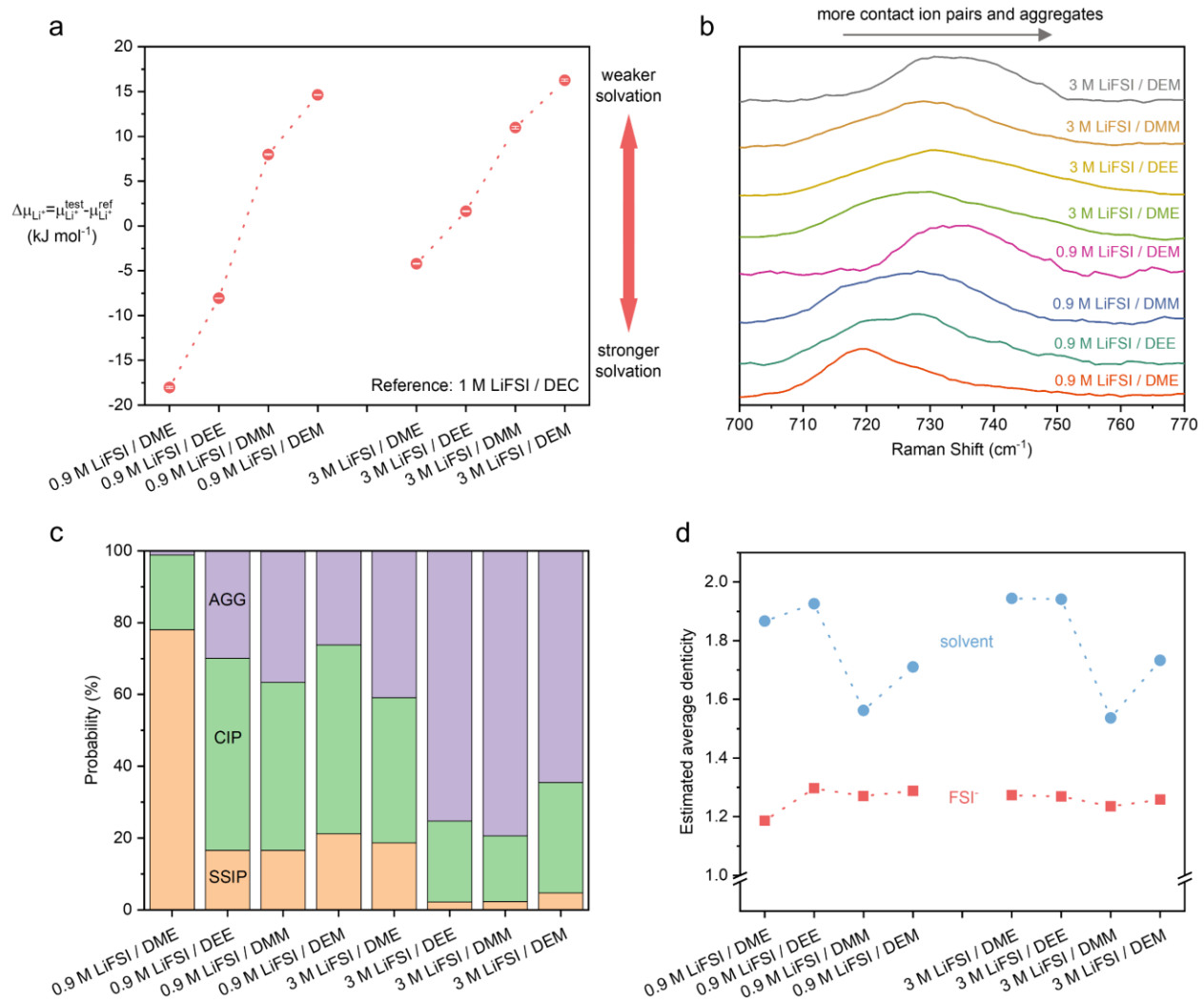


Figure 2. Experimental and computational characterizations of static solvation structures of 0.9 M and 3 M LiFSI in acetals (DMM and DEM) and ethylene glycol ethers (DME and DEE). (a) The difference in Li<sup>+</sup> chemical potential in sample electrolytes and reference electrolyte ( $\Delta\mu_{\text{Li}^+}$ ). A higher  $\Delta\mu_{\text{Li}^+}$  correlates to weaker Li<sup>+</sup> solvation at the same concentration, assuming only small contributions from the difference in activities. Three measurements were averaged for each sample with error bars shown. (b) Raman spectra of the electrolytes. The convoluted peaks between 700 and 760 cm<sup>-1</sup> correspond to FSI<sup>-</sup> in various solvation environments. The increasing wavenumbers roughly correlate to more Li<sup>+</sup>-FSI<sup>-</sup> interactions. The data of ethylene glycol ethers were reproduced from ref <sup>9</sup>. (c-d) Solvation structures by MD simulation. (c) Probability of various Li<sup>+</sup> solvation environments categorized by solvent-separated

ion pairs (SSIP) (0 FSI<sup>-</sup> around 1 Li<sup>+</sup>), contact ion pairs (CIP) (1 FSI<sup>-</sup>), and ion aggregates (AGG) ( $\geq 2$  FSI<sup>-</sup>). (d) Estimated average denticity of coordinating solvent (blue) and FSI<sup>-</sup> (red) around Li<sup>+</sup>.

The observation from  $\Delta\mu_{\text{Li}^+}$  was corroborated by the degree of ion interactions inferred from Raman spectroscopy. The data are shown in Figure 2b, where the convoluted peaks between 700 and 760 cm<sup>-1</sup> correspond to FSI<sup>-</sup> in various solvation environments. A shift to higher wavenumber indicates a greater proportion of contact ion pairs (CIP) and ion aggregates (AGG), relative to solvent-separated ion pairs (SSIP).<sup>44,45,46</sup> At both 0.9 M and 3 M, the wavenumber increases in the order of DME < DEE  $\approx$  DMM < DEM, which implies the increasing proportion of FSI<sup>-</sup> in CIP and AGG. The trend is consistent with  $\Delta\mu_{\text{Li}^+}$ , except that the Raman shifts in DEE and DMM electrolytes are comparable. A similar discrepancy has been noted previously<sup>43</sup>, which was attributed to the anion-solvent interactions<sup>47</sup>— $\Delta\mu_{\text{Li}^+}$  measurement probes Li<sup>+</sup> solvation environment whereas Raman spectroscopy probes FSI<sup>-</sup> solvation environment.

In addition, all-atom molecular dynamics (MD) simulation was carried out to provide a detailed view of the inner solvation shell (Supplementary Figure S2). The Li<sup>+</sup> solvation shells are categorized as SSIP, CIP, or AGG when the number of coordinating FSI<sup>-</sup> is 0, 1, or  $\geq 2$  (Figure 2c).<sup>9,11</sup> At the same LiFSI concentration, DEE, DMM, and DEM have more CIP and AGG compared to DME due to their weaker solvation ability. As LiFSI concentration increases, the fraction of CIP and AGG increases, indicating weaker Li<sup>+</sup> solvation. Interestingly, at both 0.9 M and 3 M, DEE, DMM, and DEM exhibit similar degrees of CIP and AGG despite their difference in  $\Delta\mu_{\text{Li}^+}$ . This is because in addition to the number of FSI<sup>-</sup> in the solvation shells, several other factors could impact  $\Delta\mu_{\text{Li}^+}$ : (1) the different enthalpic interactions between Li<sup>+</sup> and solvents (Supplementary Figure S2c), (2) the different entropic effects<sup>48</sup> due to different solvent permittivity, chelation effects, and configurational freedom in the solvation shells.

From MD results, we further estimated the average denticity of coordinating solvent and FSI<sup>-</sup> around Li<sup>+</sup> (see Method). Denticity is defined as the number of donor groups (e.g. O atoms) per ligand (e.g. DME) that bind to the central metal ion (e.g. Li<sup>+</sup>). With both 0.9 M and 3 M LiFSI, the average denticity of DME and DEE is higher than that of DMM and DEM (Figure 2d), which is consistent with our prediction of monodentate DMM and DEM versus bidentate DME, DEE by NMR and DFT (Figure 1). It is worth noting that MD simulation may have overestimated the average denticity of DMM and DEM (Supplementary Discussion 3). Nevertheless, the trend in Figure 2d clearly shows the diminished chelating ability of DMM and DEM compared to DME and DEE.

The additional insight into solvent coordination geometry is provided by the non-isothermal measurement of electrode potential temperature coefficients (TC)<sup>48</sup> at the same salt concentration. The TC is related to the entropy change ( $\Delta S$ ) of Li<sup>+</sup>/Li half-cell reaction and is affected by solvent coordination geometry and charge screening effect.<sup>48</sup> The measured TC were lower in 3 M LiFSI / DMM (1.34 mV K<sup>-1</sup>) than 3 M LiFSI / DME (1.69 mV K<sup>-1</sup>) (Supplementary Figure S3). The larger TC suggests a higher  $\Delta S$  for Li<sup>+</sup>/Li reaction in DME. This can be attributed to the more significant loss in rotational freedom of bidentate-chelated DME, in comparison to the monodentate-coordinated DMM. Since DMM (2.7)<sup>49</sup> has a lower dielectric constant than DME (7.3)<sup>50</sup>, the weaker charge screening effect is expected to lead to a higher TC and  $\Delta S$  in DMM electrolytes as more solvent molecules are organized or released around Li<sup>+</sup> during the half reaction. However, the effect from solvent coordination geometry is strong enough to overcome that of charge screening. Overall, the TC measurement provided additional experimental evidence to support the different coordination geometries proposed for the acetals and ethylene glycol ethers.

**Li cycling stability.** The benefits of weakly solvating electrolytes have been previously reported, including the preferential anion decomposition and passivation of electrode-electrolyte interfaces from the formation of inorganic-rich SEI<sup>4</sup>, increased Li<sup>+</sup>/Li equilibrium potential and weakened reduction ability<sup>43</sup>, and increased surface energy of deposited Li for lower surface/volume ratio<sup>42</sup>. These reports motivated us to further investigate the electrochemical stability of acetal electrolytes.

The Li|Cu half-cell CE of the acetal electrolytes were benchmarked against the previous state-of-the-art non-fluorinated DEE electrolyte<sup>9</sup>. In the initial 20 cycles, 0.9 M and 3 M LiFSI in DMM and DEM significantly outperformed 3 M LiFSI / DEE (Figure 3a). Remarkably, 0.9 M and 3 M LiFSI in DMM reached >99% CE within 5 and 3 cycles, respectively. This is highly desirable for anode-free LMBs, but it was only previously observed in electrolytes with fluorinated solvents<sup>11,15</sup>. In comparison, 3 M LiFSI / DEM and DEE reached >99% CE after 19 and 45 cycles, respectively (Figure 3a). Their slow activation would lead to quick loss in Li inventory in the initial cycles. The stabilized average CE calculated after the 50<sup>th</sup> cycle was above 99% for all five electrolytes tested, among which 3 M LiFSI / DMM was the highest at 99.5% (Figure 3b). The average CE at various stages of Li|Cu cycling were also calculated (Supplementary Figure S4).

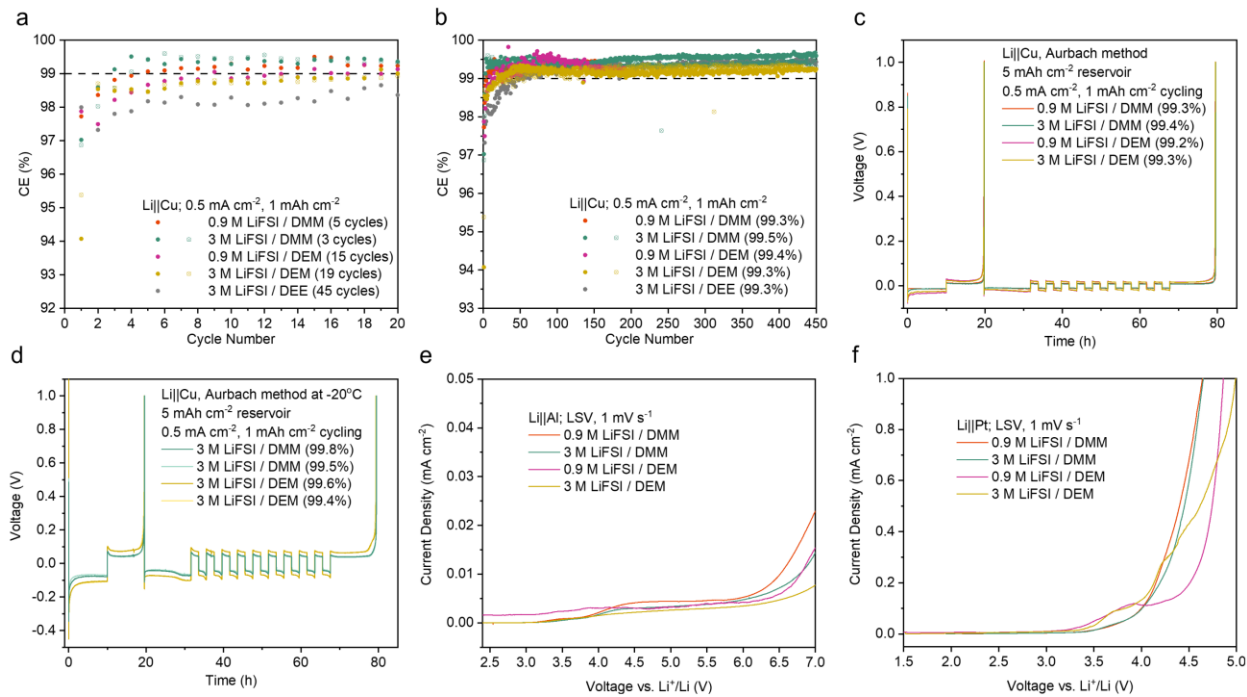


Figure 3. Electrochemical stability of 0.9 M and 3 M LiFSI in DMM and DEM. (a) Initial CE of  $\text{Li}||\text{Cu}$  cells.

The number of cycles to reach 99% is indicated for each electrolyte. (b) Long-term cycling of  $\text{Li}||\text{Cu}$  cells.

The stabilized average CEs were calculated after the 50<sup>th</sup> cycle. Abnormal cycles due to instrument

failure were omitted in the calculation. The best cell was used for calculation when there are replicates.

The data of 3 M LiFSI / DEE were taken from ref<sup>9</sup>. The average CEs at various stages of  $\text{Li}||\text{Cu}$  cycling are shown in Supplementary Figure S4. (c,d)  $\text{Li}||\text{Cu}$  CE measured by the modified Aurbach method<sup>51</sup> at room temperature (c) and  $-20^\circ\text{C}$  (d). The data for all attempted cells in (a-d) are shown in Supplementary Figure S33-35. (e,f) Oxidative stability of the electrolytes measured by LSV using Al (e) and Pt (f) as the working electrodes.

The CE was also measured by the modified Aurbach method<sup>51</sup> at room temperature (Figure 3c). With 0.9 M LiFSI, DMM (99.3%) and DEM (99.2%) both slightly outperformed DEE (99.0%)<sup>26</sup>. With 3 M LiFSI, DMM

(99.4%) and DEM (99.3%) showed similar CE as DEE (99.4%)<sup>26</sup>. The advantage of acetals compared to DEE was more apparent on bare Cu, whereas cycling on top of excess Li obscured the difference.

**Low temperature cycling.** Stable cycling (both plating and stripping) of Li at low temperatures is of great interest but rarely demonstrated.<sup>18,52,53,54</sup> We measured CEs of 3 M LiFSI in DMM, DEM and DEE by the modified Aurbach method at 0°C. Both acetal electrolytes demonstrated stable CE above 99%, whereas the DEE electrolyte showed significant instability with a large initial overpotential of ~300 mV and low CE of ~90% (Supplementary Figure S5). Notably, such instability was not due to bulk ion transport since the ionic conductivities at 0°C (with Celgard 2325) decreased in the order of DMM > DEE > DEM with 3 M LiFSI (Supplementary Figure S6a). In addition, the CEs were measured at -20°C. Compared to room temperature (Figure 3c), the CEs were higher for both acetal electrolytes at -20°C albeit slightly larger variations (Figure 3d). The increase in CE was likely due to kinetically suppressed side reactions at low temperatures. In stark contrast, 3 M LiFSI / DEE failed to achieve stable cycling at -20°C (Supplementary Figure S7) with a large initial overpotential (ca. -2.3 V) and spiky voltage.

The Li deposition morphology on Cu was observed by scanning electron microscopy (SEM) (Supplementary Figure S8, 9). For the acetal electrolytes, the Li deposition was bulky and uniform at 0°C and -20°C. In contrast, the DEE electrolyte showed bulky Li at 0°C and virtually no deposition at -20°C. If Li deposition was limited by ion transport due to low ionic conductivity of 3 M LiFSI / DEE at -20°C (Supplementary Figure S6 and notes), we would expect voltage divergence and Li dendrites<sup>55,56,57</sup>, neither of which was observed. Therefore, the poor low-temperature Li cyclability of DEE should be attributed to the slow reaction kinetics as a result of the high energy barrier for Li<sup>+</sup> de-solvation due to chelation.<sup>18,58</sup>

For comparison, the cyclability of 1.2 M LiFSI / F4DEE and F5DEE<sup>11</sup> was tested at -20°C, which showed unstable behavior (Supplementary Figure S10), further indicating the advantage of acetals over ethylene glycol ethers. Furthermore, the low-temperature cyclability was investigated in Li||Li cells (Supplementary Figure S11 and notes), which gave similar observations as Li||Cu cells.

**Oxidative stability.** A major issue of imide-based salts is their side reaction with aluminum (Al) cathode current collector at high voltages. Previously, we demonstrated that a weakly solvating electrolyte allowed the buildup of a thick and fluorine-rich passivation layer on Al even when LiFSI was used.<sup>9</sup> This was attributed to less dissolution of Al(FSI)<sub>x</sub> and other reaction products in a weakly solvating electrolyte.<sup>59</sup> Therefore, we predicted that the acetal electrolytes should be compatible with Al current collector. We performed linear scanning voltammetry (LSV) using Li||Al cells. The acetal electrolytes showed no sharp increase in leakage current below 4.4 V (Figure 3e), which indicates good stability with Al current collector. The compatibility of DMM and DEM with Al was similar to DEE and significantly better than DME with 0.9 M LiFSI (Supplementary Figure S12a). With 3 M LiFSI, all four electrolytes showed similar stability with Al within the practical voltage range (Supplementary Figure S12b).

The oxidative stability of the acetal electrolytes was also characterized by Li||Pt cells. The Pt working electrode is inert and non-reactive. Therefore, electrolyte oxidation can be captured without the passivation effect seen on Al electrode. The onset of rapid oxidation on Pt was around 4 V (versus Li<sup>+</sup>/Li) for 0.9 M and 3 M LiFSI in DMM and was slightly lower for DEM electrolytes (Figure 3f). Significant oxidation occurred at a much lower voltage range on Pt compared to Al, which indicates limited anodic stability of the acetal electrolytes despite good passivation on Al. The acetal electrolytes showed worse anodic stability on Pt compared to DME and DEE electrolytes with both 0.9 M and 3 M LiFSI

(Supplementary Figure S12c, d). Therefore, the acetal electrolytes here are not compatible with high-voltage cathodes (such as NMC) but rather more suitable with lithium iron phosphate (LFP).

**Density, viscosity, and ion transport of HCEs.** Considering the overall Li cycling stability and voltage tolerance, 3 M LiFSI / DMM and DEM appeared more suitable than the 0.9 M electrolytes for the stable operation of LMBs. We further evaluated the density and viscosity of 3 M acetal electrolytes as low density and low viscosity are desirable for practical batteries. The density of 3 M acetal is measured to be lower than 1-2 M fluorinated ethers (Supplementary Table S3), which is beneficial for the gravimetric energy density. The viscosity of 3 M acetals is lower than 3 M ethylene glycol ethers and only slightly higher than 1-2 M fluorinated ethers (Supplementary Table S3), which ensures facile wetting of cathode and separator.

The concentration-dependent ionic conductivity ( $\sigma$ ) and molar conductivity ( $\Lambda$ ) were measured (Supplementary Discussion 4 and Figure S13). Notably, in both DMM and DEM, 1.7 M and 2.4 M electrolytes have higher  $\Lambda$  than 0.9 M electrolytes, which indicates that ion transport is faster despite higher viscosity in more concentrated solutions. We will further investigate this topic in a separate publication. Overall, the  $\sigma$  of 3 M LiFSI / DMM is similar to 3 M LiFSI / DME and DEE, and is higher than 1.5 M LiFSI-1.2DME-3TTE and 1.2 M LiFSI / F4DEE and F5DEE (Supplementary Table S3). In contrast, 3 M LiFSI / DEM has a low  $\sigma$ , which limits the high-rate capability and stability.

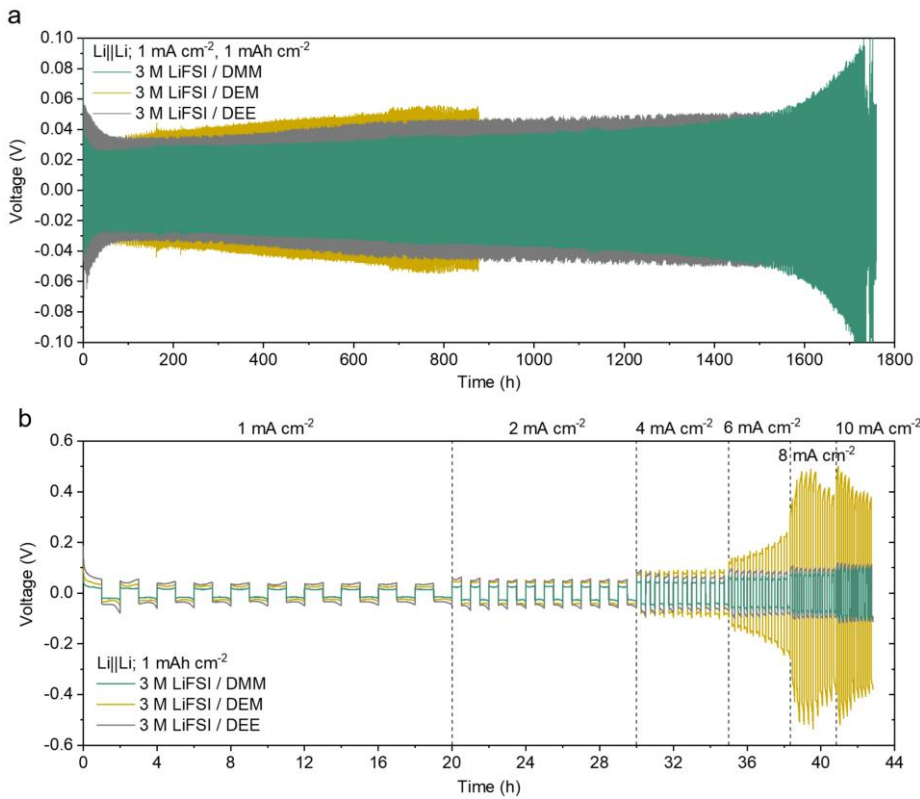


Figure 4. Voltage profiles of  $\text{Li} \parallel \text{Li}$  cells. (a) Long-term cycling at a low current density. The zoomed-in voltage curves are provided in Supplementary Figure S14a. The data of 3 M LiFSI / DEE were taken from ref<sup>9</sup>. (b) Cycling at 1 to  $10 \text{ mA cm}^{-2}$  with 10 cycles at each current density. The zoom-in voltage curves of the later cycles are provided in Supplementary Figure S14b. The data for all attempted cells are shown in Supplementary Figure S36-37.

In addition to  $\sigma$ , transport number ( $t_+$ ) is an important property that measures the current fraction under the steady state (anion-blocking condition) relative to the initial state of a  $\text{Li} \parallel \text{Li}$  cell during chronoamperometry. With both 0.9 M and 3 M LiFSI in the nonfluorinated ethers,  $t_+$  increases (DME < DEE < DMM < DEM) as the solvation ability of solvent decreases (Supplementary Table S3), which benefits the fast-charging capability.

The overpotential of Li|Li cells is a good indicator of ion transport. The cells were cycled at  $1 \text{ mA cm}^{-2}$  for  $1 \text{ mAh cm}^{-2}$  (Figure 4a and Supplementary Figure S14a). The overpotential in 3 M LiFSI / DMM was significantly lower (~22 mV after 50 cycles, ~30 mV after 800 cycles, and ~34 mV after 1200 cycles) than many reported high-CE electrolytes.<sup>15,11,60,61</sup> It was also lower than 3 M LiFSI / DEE<sup>9</sup> despite the sudden increase after 1500 hours. The overpotential in 3 M LiFSI / DEM was the highest among the three, and it increased more quickly. Electrochemical impedance spectroscopy (EIS) indicated the SEI instability contributed to the rapid increase in overpotential in 3 M LiFSI / DEM (Supplementary Discussion 5, Figure S15).

The rate capability was further tested in Li|Li cells within a current range of  $1 \text{ mA cm}^{-2}$  to  $10 \text{ mA cm}^{-2}$  (Figure 4b and Supplementary Figure S14b). Both 3 M LiFSI / DMM and DEE showed gradual increase in overpotential with current, whereas 3 M LiFSI / DEM showed a sharp increase in overpotential at  $6 \text{ mA cm}^{-2}$  due to poor ion transport. Notably, 3 M LiFSI / DMM exhibited overpotential of around 55 mV at  $6 \text{ mA cm}^{-2}$  and 85 mV at  $10 \text{ mA cm}^{-2}$ , which are among the lowest Li|Li overpotential seen in high-CE electrolytes. Overall, 3 M LiFSI / DMM showed great promise for simultaneously achieving high CE and fast  $\text{Li}^+$  transport.

**Full cell performance.** The fast activation of CE, high average CE, fast ion transport, and low overpotential make 3 M LiFSI / DMM a promising candidate for anode-free LMBs with high-rate capability. Commercial Cu|micro-LFP pouch cells (Supplementary Table S4) were tested. At C/5, C/2 and 1C charge and 2C discharge, both the DMM and DEM electrolytes achieved around 100 cycles before 80% capacity retention with good reproducibility (Figure 5a-c). The corresponding CE were above 99% with small fluctuations (Supplementary Figure S16a-c), indicating good cycling stability. In comparison to 1.2 M LiFSI / F4DEE and F5DEE<sup>11</sup>, the DMM and DEM electrolytes achieved similar cycle

life with higher capacity utilization at C/5 charge and better cycling stability at C/2 and 1C charge due to faster ion transport(Supplementary Figure S17). At 2C charge, the capacity utilization was significantly higher in 3 M LiFSI / DMM than 3 M LiFSI / DEM (Figure 5d) due to their difference in ion transport, while CE remained stable in both electrolytes (Supplementary Figure S16d). Additional Cu | | micro-LFP pouch cells were cycled at C/2 charge, 2.5C discharge and 1C charge, 1C discharge rates (Supplementary Figure S20, S18e-f and S19e). In all anode-free pouch cells above, cycle life was most likely limited by Li inventory consumption since very little overpotential increase with cycling was observed (Supplementary Figure S18-19).

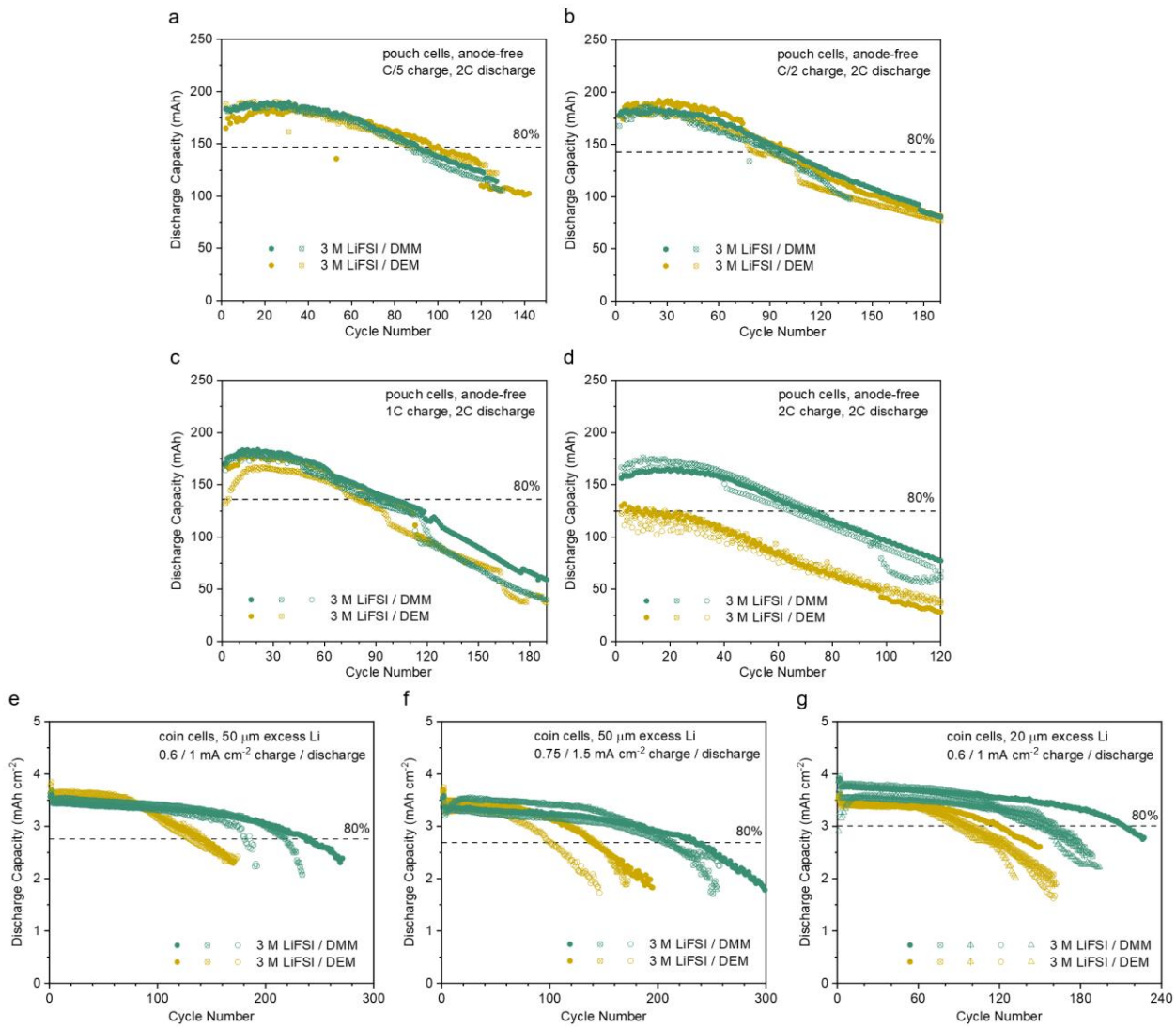


Figure 5. LFP-based full cells cycled with 3 M LiFSI / DMM and 3 M LiFSI / DEM. (a-d) Anode-free Cu| micro-LFP pouch cells (ca. 210 mAh and  $2.1 \text{ mAh cm}^{-2}$  at C/3, 2.5 to 3.65 V, 0.5 mL electrolyte, 1C = 200 mA or  $2 \text{ mA cm}^{-2}$ ) cycled at various charge rates and 2C discharge rate. The first-cycle charge rate was C/10. The 80% capacity retention line is based on the solid trace of 3 M LiFSI / DMM at the 2<sup>nd</sup> cycle. (e-g) Thin-Li| micro-LFP coin cells (3.6 to 4 mAh cm<sup>-2</sup> at <C/10, 2.5 to 3.65 V, 40  $\mu\text{L}$  electrolyte) with free-standing Li foil of 50  $\mu\text{m}$  (e, f) and 20  $\mu\text{m}$  (g) thickness cycled at various current densities. Two activation cycles were carried out at  $0.3 \text{ mA cm}^{-2}$ . The 80% capacity retention line is based on the solid trace of 3 M

LiFSI / DMM at the 4<sup>th</sup> cycle. The corresponding CE values are shown in Supplementary Figure S16. The data for every attempted cell are shown in Supplementary Figure S38.

The relatively short cycle life in anode-free cells obscured the difference in long-term stability. Therefore, thin-Li || micro-LFP coin cells were also tested using high-loading cathode (nominally 3.6 to 4 mAh cm<sup>-2</sup>) and limited excess Li (50 or 20 µm thick) cycled at 0.6 / 1 mA cm<sup>-2</sup> or 0.75 / 1.5 mA cm<sup>-2</sup> charge / discharge current densities (Figure 5e-g and Supplementary Figure S16e-g). Under the three testing conditions, 3 M LiFSI / DMM showed significantly longer cycle life than 3 M LiFSI / DEM due to higher CE and more stable overpotential (Supplementary Discussion 6).

***Limitations and future improvements.*** Despite the advantages of fast ion transport and good Li cycling stability of 3 M LiFSI / DMM, the poor oxidation stability, low boiling point, and high salt concentration necessitate further improvement in the solvent design. Compared to ethylene glycol ethers, acetal solvents clearly demonstrate superior stability with Li electrode. Therefore, by applying the concept of controlling the position and degree of fluorination<sup>11,15</sup>, we predict that the resulting fluorinated acetal solvents may simultaneously achieve good stability with high-voltage cathode and Li anode, high boiling point, reduced flammability, and fast ion transport while maintaining lower salt concentrations.<sup>62</sup> A similar concept was recently applied to diluent design.<sup>31</sup>

In addition, given the emphasis on fast charging in the battery industry, the ion transport mechanism in these highly non-ideal electrolytes deserves further investigation.<sup>63,64,65</sup> In this work, we demonstrated that a slight variation in solvent molecular structure could drastically change electrolyte conductivity and transport number, as well as their concentration-dependent trends. It is crucial to uncover the

underlying mechanism for these observations in order to address the slow ion transport problem in many advanced electrolytes to date.<sup>66</sup>

Finally, although we demonstrated the improved Li stability of DMM and DEM electrolytes compared to DEE electrolyte (Figure 3a), the detailed mechanisms for such improvement remain unclear (Supplementary Discussion 7 and related Figure S23-32). To improve from the current >99% to the required >99.99% CE for Li electrode, further investigations are required to identify the origin of small improvement among advanced electrolytes. In particular, factors beyond SEI composition and structure could be important.<sup>42,43</sup>

## Conclusion

We report solvent molecular conformation as an effective design strategy in addition to fluorine substitution<sup>11</sup> and steric effect<sup>9</sup> to control Li<sup>+</sup> solvation. Due to hyperconjugation, DMM and DEM adopt a [gauche, gauche] conformation, which makes them monodentate ligands. This leads to weaker solvation of Li<sup>+</sup> in acetals compared to ethylene glycol ethers. Consistent with previous observations in the literature, such weakly solvating electrolytes show improved Li CE. In particular, 0.9 M and 3 M LiFSI / DMM reached >99% CE within 3 to 5 cycles under our standard testing conditions, which is comparable to some of the best fluorinated ethers.<sup>11</sup> In addition, 3 M LiFSI / DMM showed low overpotentials of around 55 mV at 6 mA cm<sup>-2</sup> and 85 mV at 10 mA cm<sup>-2</sup> due to high conductivity and transport number. The fast ion transport and good Li cycling stability of 3 M LiFSI / DMM were demonstrated in anode-free Cu|LFP pouch cells as well as thin-Li|LFP coin cells. Various cell conditions and cycling procedures were used to discern the effects of ion transport, CE, and impedance growth on full-cell cycle life. Overall, we demonstrate that acetal structure is a promising alternative to ethylene glycol ether

structure for LMBs. Indeed, more recently, a fluorinated acetal was reported to enable high CEs and stable full-cell cycling even under the practical condition of fast charge and slow discharge.<sup>62</sup> Despite of improved cycling stability of acetal solvent for Li metal compared to ethylene glycol ether, their poor oxidation stability, low boiling point, and high salt concentration necessitate further improvement in the solvent design.<sup>31,62</sup> This work offers a starting point for further design and optimization of molecular analogues. Furthermore, we found the slight variations in solvent molecular structure could drastically change ion transport properties. It is crucial to investigate the ion transport mechanism to overcome the problem of slow ion transport in LMB electrolytes.<sup>66</sup> Finally, future work is needed to identify the origin of small improvement in CE above 99%. Factors beyond the extensively investigated SEI composition and structure could be fructuous.

## Methods

### *Materials*

DME (anhydrous, 99.5%, inhibitor-free) and DEM (anhydrous, 99%) were purchased from Sigma-Aldrich. DEE (99%, ACROS) and DMM (99.5%) were purchased from Fisher Scientific. LiFSI was purchased from Arkema. Celgard 2325 separator (25 µm thick, polypropylene/polyethylene/polypropylene) was purchased from Celgard. Cu current collector (25 µm thick) was purchased from Alfa Aesar. Free-standing lithium foil (600, 50 and 20 µm) was purchased from MSE Supplies. 2032-type battery casings, stainless steel spacers, springs and Al-clad coin cell cases were purchased from MTI. Micro-LFP cathode sheets were purchased from Targray. Anode-free Cu || micro-LFP pouch cells were purchased from Li-Fun Technology.

### *Solvent purification*

DEE was purified by vacuum distillation over sodium hydride. DME, DMM and DEM were not distilled.

Fresh Li foil was added to the solvents in the glovebox to further remove trace amount of water.

#### *Electrolyte preparation*

Electrolytes were prepared by dissolving 1 mmol or 4 mmol of LiFSI per 1 mL of solvent. The accurate molarities were calculated based on densities of the electrolytes, which account for the volume change upon salt dissolution.

#### *Electrochemical measurements*

2032-type coin cells with Celgard 2325 separator were used for most electrochemical measurements unless indicated otherwise. Battery fabrication was carried out in an Ar-filled glovebox. Thick Li foil (600  $\mu\text{m}$ , 1  $\text{cm}^2$ ) and 40  $\mu\text{L}$  of electrolyte were used unless otherwise specified. Electrochemical tests were carried out on Land, Arbin and Biologic systems.

Oxidation stability of electrolytes was characterized by linear sweep voltammetry on Li|Al and Li||Pt cells using Biologic MPG2. The voltage swept from open-circuit voltage to 7 V vs.  $\text{Li}^+/\text{Li}$  at a rate of 1  $\text{mV s}^{-1}$ . The leakage current density was calculated based on a working-electrode area of 2.11  $\text{cm}^2$ .

Coulombic efficiencies were measured by a modified Aurbach method<sup>51</sup> on Li|Cu cells at ambient temperature, 0°C or -20°C. The Cu surface was conditioned by plating 5  $\text{mAh cm}^{-2}$  of Li and stripping to 1 V. Then, a Li reservoir of 5  $\text{mAh cm}^{-2}$  was plated onto Cu, followed by 10 cycles of Li plating and stripping at 1  $\text{mAh cm}^{-2}$ . Finally, all Li on Cu was stripped to 1 V. The current density was 0.5  $\text{mA cm}^{-2}$  for all steps.

For the long-term cycling of Li|Cu cells, the Cu surface was conditioned by holding at 10 mV vs.  $\text{Li}^+/\text{Li}$  for 5 hours, and then cycling between 0 and 1 V at 0.2  $\text{mA cm}^{-2}$  for 10 cycles. During subsequent cycling, 1  $\text{mAh cm}^{-2}$  of Li was plated onto Cu and was then stripped to 1 V at 0.5  $\text{mA cm}^{-2}$ .

Li||Li symmetric cells were cycled at  $1 \text{ mA cm}^{-2}$  for  $1 \text{ mAh cm}^{-2}$ . In some cells, electrochemical impedance spectroscopy was carried out every 120 cycles to track the evolution of cell impedance. In addition, Li||Li cells were also cycled for  $1 \text{ mAh cm}^{-2}$  with a stepwise increase in current density every 10 cycles from  $1 \text{ mA cm}^{-2}$  to  $10 \text{ mA cm}^{-2}$ . Some Li||Li cells were also cycled at  $-20^\circ\text{C}$  at  $0.5 \text{ mA cm}^{-2}$  and  $1 \text{ mAh cm}^{-2}$  for 10 cycles.

Li||LFP coin cells were assembled using 50 or  $20 \mu\text{m}$  free-standing Li and  $40 \mu\text{L}$  of electrolyte. Al-clad cathode cases were used. Al foil was placed inside the cathode cases to avoid defects in the Al cladding. A high-loading micro-LFP cathode was used. The cells were cycled between 2.5 and  $3.65 \text{ V}$ . Two activation cycles were carried out at  $0.3 \text{ mA cm}^{-2}$ , which produced second-cycle discharge capacities between  $3.6$  and  $4 \text{ mAh cm}^{-2}$  due to slight variations in the cathode loading. Long-term cycling was carried out at  $0.6 / 1 \text{ mA cm}^{-2}$  or  $0.75 / 1.5 \text{ mA cm}^{-2}$  charge / discharge current densities.

Anode-free Cu||micro-LFP dry pouch cells were factory manufactured (ca.  $210 \text{ mAh}$  and  $2.1 \text{ mAh cm}^{-2}$  at C/3). The electrolyte ( $0.5 \text{ mL}$ ) was injected and the pouch was re-sealed under vacuum. Vises and polycarbonate plates were used to apply ca.  $1000 \text{ kPa}$  pressure to the pouch cells. The cells were cycled under ambient temperature between 2.5 and  $3.65 \text{ V}$  at various charge and discharge rates (1C =  $200 \text{ mA}$  or  $2 \text{ mA cm}^{-2}$ ). The first-cycle charge rate was C/10.

Ionic conductivities were measured by electrochemical impedance spectroscopy. Swagelok-type cell with symmetric stainless-steel electrodes and without separator was used to measure the intrinsic electrolyte conductivity at ambient temperature. 2032-type coin cells with symmetric stainless-steel electrodes and Celgard 2325 separator were used to measure temperature-dependent ionic conductivity in the presence of separator.

Transport number was measured by the Vincent-Bruce method in Li||Li symmetric cells with a modified procedure.<sup>67</sup> The interface was stabilized by 5 cycles at  $0.5 \text{ mA cm}^{-2}$  for  $1 \text{ mAh cm}^{-2}$ .

Chronoamperometry (CA) was carried out at 10 mV until the steady-state current was achieved. EIS was carried out before and after the CA step to account for changes in interfacial resistance.

The measurement of  $\Delta E_{\text{eq}}^{\text{Li}^+/\text{Li}}$  was previously developed by our groups.<sup>41</sup> The home-made apparatus consisted of three chambers, each containing a different electrolyte (test, reference or salt-bridge electrolyte), and two porous junctions that separate the three chambers. Four layers of Celgard 2325 separator were used as the porous junction. Two pieces of fresh lithium foil were used as electrodes. The cell voltage was measured by Biologic VMP3. The voltage was recorded after stabilization, which typically takes up to three minutes.

The non-isothermal measurement of electrode potential temperature coefficients was previously developed by our groups.<sup>48</sup> An H-cell with a porous frit was used. Two pieces of fresh lithium foil were used as electrodes, and the same electrolyte was used on both sides. A thermocouple (Omega, HSTCTT-K-24S-36) was installed in each half cell adjacent to the electrode surface to measure the temperature of the electrolyte/electrode interface using a temperature scanner (Omega, DP1001AM). A Kapton heater was wrapped around one side of the H-cell to provide uniform heating. During the measurement, the heating power was adjusted via a potentiostat (BioLogic VMP3). For each heating power set point, the stabilized temperature and open-circuit voltage were recorded.

#### *Materials characterizations*

NMR was performed on Varian 400 MHz spectrometer at 25°C. The  ${}^1\text{J}_{\text{CH}}$  coupling constants of anomeric  $\text{CH}_2$  group of DMM, DEM, and DOL were extracted from 1D  ${}^1\text{H}$  NMR spectra at various LiFSI and LiTFSI concentrations.  ${}^7\text{Li}$  pulsed field gradient (PFG) measurements were performed to determine the self-diffusion coefficients of  $\text{Li}^+$  using dbppste\_cc pulse sequence. Array of gradient strength was set to 2.908 to 12.504 G cm<sup>-1</sup> with 12 linear steps. Appropriate diffusion delay ( $\Delta$ ) and gradient pulse duration ( $\delta$ )

were selected to ensure sufficient signal decay. Self-diffusion coefficients were calculated by fitting peak integrals to the Stejskal–Tanner equation.

Raman spectra were collected on a Horiba XploRA+ confocal Raman with 532 nm excitation laser. The electrolytes were sealed under argon in quartz cuvettes.

Viscosity measurements were carried out using an Ares G2 rheometer (TA Instruments) with an advanced Peltier system at 25.0 °C.

Differential scanning calorimetry was carried out on TA Instrument Q2500. Aluminum hermetic pans were used. The temperature was scanned to 25°C first, followed by cooling to -75°C and then heating. The ramp was 10°C min<sup>-1</sup> for all steps.

The physical state of electrolytes was observed after equilibrating for at least 2 hours at 0°C, -20°C and -80°C in a temperature chamber or freezer.

The surface morphology of Li was imaged by FEI Magellan 400 XHR scanning electron microscope. In Li|Cu cells, the Cu electrode was pre-conditioned by holding at 0.01 V for 5 hours, and then cycling between 0 and 1 V at 0.2 mA cm<sup>-2</sup> for 10 cycles. Li was deposited on Cu at 0.5 mA cm<sup>-2</sup> for 0.5 mAh cm<sup>-2</sup>. After deposition, the cells were disassembled, and the electrodes were rinsed with 80 µL of the corresponding pure solvents. The Li deposition morphology at 0°C and -20°C was also imaged after depositing Li at 0.5 mA cm<sup>-2</sup> for 5 mAh cm<sup>-2</sup> in Li|Cu cells. In addition, Li electrode morphology in Li||Li cells cycled at -20°C was characterized (0.5 mA cm<sup>-2</sup> and 1 mAh cm<sup>-2</sup> for 10 cycles).

The Li deposition morphology in the presence of rSEI was imaged by FEI Magellan 400 XHR scanning electron microscope. The Li|Cu cells were pre-conditioned at 0.2 mA cm<sup>-2</sup> between 0 and 1 V for 10 cycles, followed by 10 cycles at 0.5 mA cm<sup>-2</sup> and 1 mAh cm<sup>-2</sup> plating and 0.5 mA cm<sup>-2</sup> stripping to 1 V to form rSEI. In the final step, 0.1, 0.5 or 1 mAh cm<sup>-2</sup> capacity was plated at 0.5 mA cm<sup>-2</sup>. The Cu electrodes

were rinsed with 80  $\mu$ L of the corresponding pure solvents before imaging. Alternatively, the 50- $\mu$ m-Li|thick-Li cells were pre-cycled at 0.4 mA cm<sup>-2</sup> for 2 cycles, followed by 10 cycles at 0.4 or 4 mA cm<sup>-2</sup> plating and 4 mA cm<sup>-2</sup> stripping, with 4 mAh cm<sup>-2</sup> in each step to form rSEI. In the final step, 0.2, 1 or 4 mAh cm<sup>-2</sup> capacity was plated at 0.4 or 4 mA cm<sup>-2</sup>. The 50- $\mu$ m-Li electrodes were rinsed with 80  $\mu$ L of the corresponding pure solvents before imaging.

The cross sections of rSEI were imaged by FEI Helios NanoLab 600i DualBeam SEM/FIB. Li|Cu cells were cycled at 0.5 mA cm<sup>-2</sup> for 1 mAh cm<sup>-2</sup> for 10 cycles. The active Li was stripped in the final step, leaving rSEI on Cu substrate. An air-free transfer vessel was used. Pt was deposited to preserve the top surface of rSEI. Cross sections were prepared by Ga<sup>+</sup> ion beam.

A ThermoFisher Titan 80-300 environmental transmission electron microscope at an accelerating voltage of 300 kV and a Gatan 626 side-entry holder were used for cryo-TEM and cryo-EDS experiments. Cryo-TEM sample preparations prevent air and moisture exposure and reduce electron beam damage, as described previously<sup>68,69</sup>. The TEM is equipped with an aberration corrector in the image-forming lens, which was tuned before imaging. Cryo-TEM images were acquired by a Gatan K3 IS direct-detection camera in the electron-counting mode. Cryo-TEM images were taken with an electron dose rate of around 100 e<sup>-</sup> Å<sup>-2</sup> s<sup>-1</sup>, and a total of five frames were taken with 0.1 s per frame for each image. The samples were prepared by depositing 0.2 mAh of Li on bare Cu grid at 1 mA cm<sup>-2</sup>.

PHI VersaProbe 3 XPS with monochromatized Al(Ka) Source (1486 eV) and focused ion gun was used to characterize SEI compositions after cycling. An air-tight vessel was used to transfer samples without exposure to air. The samples were sputtered for 1 min to get rid of adventitious carbon. Li|Cu cells were first pre-conditioned at 0.2 mA cm<sup>-2</sup> between 0 and 1 V for 10 cycles, followed by 10 cycles at 0.5 mA cm<sup>-2</sup> plating for 1 mAh cm<sup>-2</sup> and 0.5 mA cm<sup>-2</sup> stripping to 1 V. The fully stripped Cu electrodes were rinsed with 80  $\mu$ L of the corresponding pure solvents before XPS.

### *Theoretical calculations*

Density functional theory (DFT) with the hybrid exchange-correlation functional B3LYP<sup>70</sup> with the Becke-Johnson damping scheme (D3BJ)<sup>71,72</sup> was applied for the geometry optimization, and all DFT calculations were performed with the def2-TZVP basis set<sup>73</sup> using ORCA package<sup>74</sup>.

MD simulations were carried out using Gromacs 2021.3<sup>75</sup> with the general amber force field (GAFF)<sup>76</sup>. Topology files were generated using ACPYPE<sup>77</sup>, and the atomic partial charges were calculated by the restrained electrostatic potential (RESP) fitting approach in antechamber 22.0<sup>78</sup>, where the quantum mechanical molecular electrostatic potential was computed by Gaussian16 at the B3LYP/6-311\*\* level<sup>79</sup>. To improve the accuracy of the non-polarizable force field, partial charges for charged ions were scaled by factors ranging from 0.6 to 0.72 to account for electronic screening. The scaling factors were adjusted to match the diffusion coefficients measured by the experiments (Supplementary Table S2).

To compute the diffusivity coefficient through the NVT molecular dynamics simulations, molecular dynamics was first equilibrated for 2 ns using Parrinello-Rahman barostat at a reference pressure of 1 bar. The simulation size box for the following NVT simulations was determined by the average size in the last 1 ns. After that, 2 ns equilibration step was followed by 80 ns production run with fixed volume. A Nosé-Hoover thermostat was used throughout with a reference temperature of 300 K. The particle mesh Ewald method was used to calculate electrostatic interactions, with a real space cutoff of 1.0 nm and a Fourier spacing of 0.16 nm. The Verlet cutoff scheme was used to generate pair lists. A cutoff of 1.0 nm was used for non-bonded Lennard-Jones interactions. Periodic boundary conditions were applied in all directions. Bonds with hydrogen atoms were constrained. The trajectories of the production run were used for the analysis.

The visualizations were generated with VMD.<sup>80</sup> Solvation shell statistics were calculated using the MDAnalysis Python package<sup>81</sup> by histogramming the observed first solvation shells for lithium ions during

the production simulation, using a method similar to previous work.<sup>11,15</sup> The cutoff distance for each species in the first solvation shell was calculated from the first minimum occurring in the RDF (referenced to lithium ions) after the initial peak. The average numbers of coordinating species in the solvation shell of Li<sup>+</sup> were calculated by counting (1) solvent molecules and anions and (2) oxygen atoms on solvent molecules and anions. Their ratio was taken as a rough indicator of coordination denticity.

### Acknowledgement

The work was supported by the Assistant Secretary for Energy Efficiency and Renewable Energy, Office of Vehicle Technologies of the U.S. Department of Energy under the Battery 500 Consortium program, and Stanford Precourt Institute for Energy under the StorageX Initiative Seed Grants. Y.Cui acknowledges the cryo-EM support from the U.S. Department of Energy (DOE), Office of Basic Energy Sciences, Division of Materials Sciences and Engineering (Contract No. DE-AC02-76SF00515). Y.Chen acknowledges the support from Chevron Fellowship. S.L. acknowledges the support from LEAP Fellowship. Part of this work was performed at the Stanford Nano Shared Facilities (SNSF), supported by the National Science Foundation under Award ECCS-2026822. DFT and MD calculations were performed on the Sherlock cluster. We would like to thank Stanford University and the Stanford Research Computing Center for providing computational resources and support that contributed to these research results.

### Author contributions

Y.Chen conceived the idea. Y.Chen and S.L. designed the study. Z.B., J.Q., and Y.Cui directed the project. Y.Chen performed electrochemical experiments, cell testing, NMR, SEM, and DSC. S.L. performed MD

and DFT calculations. H.G. performed SEM and XPS. Z.Z. performed cryo-EM and EDS. Z.H. performed Raman spectroscopy and viscosity measurement. S.C.K performed Li<sup>+</sup> chemical potential and electrode potential temperature coefficients measurements. E.Z. and W.Y. performed XPS. H.L. performed FIB-SEM. Y.L. and P.S. contributed to key discussions. All authors contributed to the analysis, interpretation, and discussion of the data. Y.Chen, S.L., Z.B., J.Q., and Y.Cui wrote and revised the manuscript.

## Notes

The authors declare the following competing financial interest(s): 1,2-diethoxyethane, dimethoxymethane, and diethoxymethane electrolytes have been filed as International Patent Application No. PCT/US2022/47472; fluorinated diethoxymethane electrolytes have been filed as International Patent Application No. PCT/US2023/021234.

## References

- (1) Hobold, G. M.; Lopez, J.; Guo, R.; Minafra, N.; Banerjee, A.; Shirley Meng, Y.; Shao-Horn, Y.; Gallant, B. M. Moving beyond 99.9% Coulombic Efficiency for Lithium Anodes in Liquid Electrolytes. *Nat. Energy* **2021**, 6 (10), 951–960. <https://doi.org/10.1038/s41560-021-00910-w>.
- (2) Kim, S.; Park, G.; Lee, S. J.; Seo, S.; Ryu, K.; Kim, C. H.; Choi, J. W. Lithium Metal Batteries: From Fundamental Research to Industrialization. *Adv. Mater.* **2023**, 2206625, 1–20. <https://doi.org/10.1002/adma.202206625>.
- (3) Lin, D.; Liu, Y.; Cui, Y. Reviving the Lithium Metal Anode for High-Energy Batteries. *Nat. Nanotechnol.* **2017**, 12 (3), 194–206. <https://doi.org/10.1038/nnano.2017.16>.

- (4) Wang, H.; Yu, Z.; Kong, X.; Kim, S. C.; Boyle, D. T.; Qin, J.; Bao, Z.; Cui, Y. Liquid Electrolyte: The Nexus of Practical Lithium Metal Batteries. *Joule* **2022**, *6* (3), 588–616.  
<https://doi.org/10.1016/j.joule.2021.12.018>.
- (5) Niu, C.; Liu, D.; Lochala, J. A.; Anderson, C. S.; Cao, X.; Gross, M. E.; Xu, W.; Zhang, J. G.; Whittingham, M. S.; Xiao, J.; et al. Balancing Interfacial Reactions to Achieve Long Cycle Life in High-Energy Lithium Metal Batteries. *Nat. Energy* **2021**, *6* (7), 723–732.  
<https://doi.org/10.1038/s41560-021-00852-3>.
- (6) Fan, X.; Chen, L.; Borodin, O.; Ji, X.; Chen, J.; Hou, S.; Deng, T.; Zheng, J.; Yang, C.; Liou, S. C.; et al. Non-Flammable Electrolyte Enables Li-Metal Batteries with Aggressive Cathode Chemistries. *Nat. Nanotechnol.* **2018**, *13* (8), 715. <https://doi.org/10.1038/s41565-018-0183-2>.
- (7) Weber, R.; Genovese, M.; Louli, A. J.; Hames, S.; Martin, C.; Hill, I. G.; Dahn, J. R. Long Cycle Life and Dendrite-Free Lithium Morphology in Anode-Free Lithium Pouch Cells Enabled by a Dual-Salt Liquid Electrolyte. *Nat. Energy* **2019**, *4* (8), 683–689. <https://doi.org/10.1038/s41560-019-0428-9>.
- (8) Louli, A. J.; ElDesoky, A.; Weber, R.; Genovese, M.; Coon, M.; deGooyer, J.; Deng, Z.; White, R. T.; Lee, J.; Rodgers, T.; et al. Diagnosing and Correcting Anode-Free Cell Failure via Electrolyte and Morphological Analysis. *Nat. Energy* **2020**, *5* (9), 693–702. <https://doi.org/10.1038/s41560-020-0668-8>.
- (9) Chen, Y.; Yu, Z.; Rudnicki, P.; Gong, H.; Huang, Z.; Kim, S. C.; Lai, J.-C.; Kong, X.; Qin, J.; Cui, Y.; et al. Steric Effect Tuned Ion Solvation Enabling Stable Cycling of High-Voltage Lithium Metal Battery. *J. Am. Chem. Soc.* **2021**, *143* (44), 18703–18713. <https://doi.org/10.1021/jacs.1c09006>.
- (10) Kim, M. S.; Zhang, Z.; Rudnicki, P. E.; Yu, Z.; Wang, J.; Wang, H.; Oyakhire, S. T.; Chen, Y.; Kim, S. C.; Zhang, W.; et al. Suspension Electrolyte with Modified Li<sup>+</sup> Solvation Environment for Lithium

Metal Batteries. *Nat. Mater.* **2022**, *21*, 445–454. <https://doi.org/10.1038/s41563-021-01172-3>.

- (11) Yu, Z.; Rudnicki, P. E.; Zhang, Z.; Huang, Z.; Celik, H.; Oyakhire, S. T.; Chen, Y.; Kong, X.; Kim, S. C.; Xiao, X.; et al. Rational Solvent Molecule Tuning for High-Performance Lithium Metal Battery Electrolytes. *Nat. Energy* **2022**, *7* (1), 94–106. <https://doi.org/10.1038/s41560-021-00962-y>.
- (12) Zhang, H.; Zeng, Z.; He, R.; Wu, Y.; Hu, W.; Lei, S.; Liu, M.; Cheng, S.; Xie, J. 1,3,5-Trifluorobenzene and Fluorobenzene Co-Assisted Electrolyte with Thermodynamic and Interfacial Stabilities for High-Voltage Lithium Metal Battery. *Energy Storage Mater.* **2022**, *48* (November 2021), 393–402. <https://doi.org/10.1016/j.ensm.2022.03.034>.
- (13) Yoo, D.; Yang, S.; Kim, K. J.; Choi, J. W. Fluorinated Aromatic Diluent for High-Performance Lithium Metal Batteries. *Angew. Chemie* **2020**, *132* (35), 14979–14986. <https://doi.org/10.1002/ange.202003663>.
- (14) Eldesoky, A.; Louli, A. J.; Benson, A.; Dahn, J. R. Cycling Performance of NMC811 Anode-Free Pouch Cells with 65 Different Electrolyte Formulations. *J. Electrochem. Soc.* **2021**, *168* (12), 120508. <https://doi.org/10.1149/1945-7111/ac39e3>.
- (15) Yu, Z.; Wang, H.; Kong, X.; Huang, W.; Tsao, Y.; Mackanic, D. G.; Wang, K.; Wang, X.; Huang, W.; Choudhury, S.; et al. Molecular Design for Electrolyte Solvents Enabling Energy-Dense and Long-Cycling Lithium Metal Batteries. *Nat. Energy* **2020**, *5* (7), 526–533. <https://doi.org/10.1038/s41560-020-0634-5>.
- (16) Qian, J.; Henderson, W. A.; Xu, W.; Bhattacharya, P.; Engelhard, M.; Borodin, O.; Zhang, J. G. High Rate and Stable Cycling of Lithium Metal Anode. *Nat. Commun.* **2015**, *6*, 6362. <https://doi.org/10.1038/ncomms7362>.
- (17) Ren, X.; Zou, L.; Cao, X.; Engelhard, M. H.; Liu, W.; Burton, S. D.; Lee, H.; Niu, C.; Matthews, B. E.;

Zhu, Z.; et al. Enabling High-Voltage Lithium-Metal Batteries under Practical Conditions. *Joule* **2019**, *3* (7), 1662–1676. <https://doi.org/10.1016/j.joule.2019.05.006>.

- (18) Holoubek, J.; Liu, H.; Wu, Z.; Yin, Y.; Xing, X.; Cai, G.; Yu, S.; Zhou, H.; Pascal, T. A.; Chen, Z.; et al. Tailoring Electrolyte Solvation for Li Metal Batteries Cycled at Ultra-Low Temperature. *Nat. Energy* **2021**, *6*, 303–313. <https://doi.org/10.1038/s41560-021-00783-z>.
- (19) Liu, H.; Holoubek, J.; Zhou, H.; Chen, A.; Chang, N.; Wu, Z.; Yu, S.; Yan, Q.; Xing, X.; Li, Y.; et al. Ultrahigh Coulombic Efficiency Electrolyte Enables Li||SPAN Batteries with Superior Cycling Performance. *Mater. Today* **2021**, *42* (xx), 17–28. <https://doi.org/10.1016/j.mattod.2020.09.035>.
- (20) Huang, F.; Ma, G.; Wen, Z.; Jin, J.; Xu, S.; Zhang, J. Enhancing Metallic Lithium Battery Performance by Tuning the Electrolyte Solution Structure. *J. Mater. Chem. A* **2018**, *6* (4), 1612–1620. <https://doi.org/10.1039/c7ta08274f>.
- (21) Lee, M. S.; Roev, V.; Jung, C.; Kim, J. R.; Han, S.; Kang, H. R.; Im, D.; Kim, I. S. An Aggregate Cluster-Dispersed Electrolyte Guides the Uniform Nucleation and Growth of Lithium at Lithium Metal Anodes. *ChemistrySelect* **2018**, *3* (41), 11527–11534. <https://doi.org/10.1002/slct.201800757>.
- (22) Xue, W.; Huang, M.; Li, Y.; Zhu, Y. G.; Gao, R.; Xiao, X.; Zhang, W.; Li, S.; Xu, G.; Yu, Y.; et al. Ultra-High-Voltage Ni-Rich Layered Cathodes in Practical Li Metal Batteries Enabled by a Sulfonamide-Based Electrolyte. *Nat. Energy* **2021**, *6*, 495–505. <https://doi.org/10.1038/s41560-021-00792-y>.
- (23) Niu, C.; Liu, D.; Lochala, J. A.; Anderson, C. S.; Cao, X.; Gross, M. E.; Xu, W.; Zhang, J.; Whittingham, M. S.; Xiao, J.; et al. Balancing Interfacial Reactions to Achieve Long Cycle Life in High-Energy Lithium Metal Batteries. *Nat. Energy* **2021**. <https://doi.org/10.1038/s41560-021-00852-3>.
- (24) Zhang, Z.; Li, Y.; Xu, R.; Zhou, W.; Li, Y.; Oyakhire, S. T.; Wu, Y.; Xu, J.; Wang, H.; Yu, Z.; et al.

Capturing the Swelling of Solid-Electrolyte Interphase in Lithium Metal Batteries. *Science* (80-. ).  
**2022**, 375 (6576), 66–70. <https://doi.org/10.1126/science.abi8703>.

- (25) Sayavong, P.; Zhang, W.; Oyakhire, S. T.; Boyle, D. T.; Chen, Y.; Kim, S. C.; Vilá, R. A.; Holmes, S. E.; Kim, M. S.; Bent, S. F.; et al. Dissolution of the Solid Electrolyte Interphase and Its Effects on Lithium Metal Anode Cyclability. *J. Am. Chem. Soc.* **2023**, 145 (22), 12342–12350.  
<https://doi.org/10.1021/jacs.3c03195>.
- (26) Chen, Y.; Yu, Z.; Rudnicki, P.; Gong, H.; Huang, Z.; Kim, S. C.; Lai, J. C.; Kong, X.; Qin, J.; Cui, Y.; et al. Steric Effect Tuned Ion Solvation Enabling Stable Cycling of High-Voltage Lithium Metal Battery. *J. Am. Chem. Soc.* **2021**, 143 (44), 18703–18713. <https://doi.org/10.1021/jacs.1c09006>.
- (27) Li, Z.; Rao, H.; Atwi, R.; Sivakumar, B. M.; Gwalani, B.; Gray, S.; Han, K. S.; Everett, T. A.; Ajantiwalay, T. A.; Murugesan, V.; et al. Non-Polar Ether-Based Electrolyte Solutions for Stable High-Voltage Non-Aqueous Lithium Metal Batteries. *Nat. Commun.* **2023**, 14 (1).  
<https://doi.org/10.1038/s41467-023-36647-1>.
- (28) Li, G. X.; Koverga, V.; Nguyen, A.; Kou, R.; Ncube, M.; Jiang, H.; Wang, K.; Liao, M.; Guo, H.; Chen, J.; et al. Enhancing Lithium-Metal Battery Longevity through Minimized Coordinating Diluent. *Nat. Energy* **2024**. <https://doi.org/10.1038/s41560-024-01519-5>.
- (29) Zhang, G.; Chang, J.; Wang, L.; Li, J.; Wang, C.; Wang, R.; Shi, G.; Yu, K.; Huang, W.; Zheng, H.; et al. A Monofluoride Ether-Based Electrolyte Solution for Fast-Charging and Low-Temperature Non-Aqueous Lithium Metal Batteries. *Nat. Commun.* **2023**, 14 (1), 1–13.  
<https://doi.org/10.1038/s41467-023-36793-6>.
- (30) Ruan, D.; Tan, L.; Chen, S.; Fan, J.; Nian, Q.; Chen, L.; Wang, Z.; Ren, X. Solvent versus Anion Chemistry: Unveiling the Structure-Dependent Reactivity in Tailoring Electrochemical Interphases

for Lithium-Metal Batteries. *JACS Au* **2023**, *3* (3), 953–963.

<https://doi.org/10.1021/jacsau.3c00035>.

- (31) Zhao, Y.; Zhou, T.; Jeurgens, P. H.; Kong, X.; Choi, W.; Coskun, A. Electrolyte Engineering for Highly Inorganic Solid Electrolyte Interphase in High-Performance Lithium Metal Batteries. *Chem* **2023**, *9*, 1–16. <https://doi.org/10.1016/j.chempr.2022.12.005>.
- (32) Zhao, Y.; Zhou, T.; Mensi, M.; Choi, J. W.; Coskun, A. Electrolyte Engineering via Ether Solvent Fluorination for Developing Stable Non-Aqueous Lithium Metal Batteries. *Nat. Commun.* **2023**, *14*, 299. <https://doi.org/10.1038/s41467-023-35934-1>.
- (33) Ma, T.; Ni, Y.; Wang, Q.; Zhang, W.; Jin, S.; Zheng, S.; Yang, X.; Hou, Y.; Tao, Z.; Chen, J. Optimize Lithium Deposition at Low Temperature by Weakly Solvating Power Solvent. *Angew. Chemie - Int. Ed.* **2022**, *300071*. <https://doi.org/10.1002/anie.202207927>.
- (34) Ding, K.; Xu, C.; Peng, Z.; Long, X.; Shi, J.; Li, Z.; Zhang, Y.; Lai, J.; Chen, L.; Cai, Y.; et al. Tuning the Solvent Alkyl Chain to Tailor Electrolyte Solvation for Stable Li-Metal Batteries. *ACS Appl. Mater. Interfaces* **2022**. <https://doi.org/10.1021/acsami.2c13517>.
- (35) Flamme, B.; Rodriguez Garcia, G.; Weil, M.; Haddad, M.; Phansavath, P.; Ratovelomanana-Vidal, V.; Chagnes, A. Guidelines to Design Organic Electrolytes for Lithium-Ion Batteries: Environmental Impact, Physicochemical and Electrochemical Properties. *Green Chem.* **2017**, *19* (8), 1828–1849. <https://doi.org/10.1039/c7gc00252a>.
- (36) Carey, F. A.; Sundberg, R. J. *Advanced Organic Chemistry*, 5th ed.; Springer: New York, 2007.
- (37) Abe, A.; Inomata, K.; Tanisawa, E.; Ando, I. Conformation and Conformational Energies of Dimethoxymethane and 1,1-Dimethoxyethane. *J. Mol. Struct.* **1990**, *238*, 315–323.
- (38) Anderson, J. E.; Heki, K.; Hirota, M.; Jørgensen, F. S. Setting the Anomeric Effect against Steric

Effects in Simple Acyclic Acetals. Non-Anomeric Non-Classical Conformations. An N.M.R. and Molecular Mechanics Investigation. *J. Chem. Soc. Chem. Commun.* **1987**, No. 8, 554–555.  
<https://doi.org/10.1039/C39870000554>.

- (39) Tvaroska, I.; Taravel, F. R. Carbon-Proton Coupling Constants in the Conformational Analysis of Sugar Molecules. In *Advances in Carbohydrate Chemistry and Biochemistry*; 1995; Vol. 51, pp 15–61. [https://doi.org/10.1016/S0065-2318\(08\)60191-2](https://doi.org/10.1016/S0065-2318(08)60191-2).
- (40) Lemieux, R. U.; Stevens, J. D.; Fraser, R. R. Observations on the Karplus Curve in Relation To the Conformation of the 1,3-Dioxolane Ring. *Can. J. Chem.* **1962**, 40 (10), 1955–1959.  
<https://doi.org/10.1139/v62-300>.
- (41) Kim, S. C.; Kong, X.; Vilá, R. A.; Huang, W.; Chen, Y.; Boyle, D. T.; Yu, Z.; Wang, H.; Bao, Z.; Qin, J.; et al. Potentiometric Measurement to Probe Solvation Energy and Its Correlation to Lithium Battery Cyclability. *J. Am. Chem. Soc.* **2021**, 143 (27), 10301–10308.  
<https://doi.org/10.1021/jacs.1c03868>.
- (42) Boyle, D. T.; Kim, S. C.; Oyakhire, S. T.; Vila, R. A.; Huang, Z.; Sayavong, P.; Qin, J.; Bao, Z.; Cui, Y. Correlating Kinetics to Cyclability Reveals Thermodynamic Origin of Lithium Anode Morphology in Liquid Electrolytes. *J. Am. Chem. Soc.* **2022**. <https://doi.org/10.1021/jacs.2c08182>.
- (43) Ko, S.; Obukata, T.; Shimada, T.; Takenaka, N.; Nakayama, M.; Yamada, A.; Yamada, Y. Electrode Potential Influences the Reversibility of Lithium-Metal Anodes. *Nat. Enrgy* **2022**.  
<https://doi.org/10.1038/s41560-022-01144-0>.
- (44) Yamada, Y.; Yaegashi, M.; Abe, T.; Yamada, A. A Superconcentrated Ether Electrolyte for Fast-Charging Li-Ion Batteries. *Chem. Commun.* **2013**, 49, 11194–11196.  
<https://doi.org/10.1039/c3cc46665e>.

- (45) Cao, X.; Zou, L.; Matthews, B. E.; Zhang, L.; He, X.; Ren, X.; Engelhard, M. H.; Burton, S. D.; El-Khoury, P. Z.; Lim, H. S.; et al. Optimization of Fluorinated Orthoformate Based Electrolytes for Practical High-Voltage Lithium Metal Batteries. *Energy Storage Mater.* **2021**, *34*, 76–84. <https://doi.org/10.1016/j.ensm.2020.08.035>.
- (46) Jiang, Z.; Zeng, Z.; Liang, X.; Yang, L.; Hu, W.; Zhang, C.; Han, Z.; Feng, J.; Xie, J. Fluorobenzene, A Low-Density, Economical, and Bifunctional Hydrocarbon Cosolvent for Practical Lithium Metal Batteries. *Adv. Funct. Mater.* **2021**, *31*, 2005991. <https://doi.org/10.1002/adfm.202005991>.
- (47) Popov, I.; Sacci, R. L.; Sanders, N. C.; Matsumoto, R. A.; Thompson, M. W.; Osti, N. C.; Kobayashi, T.; Tyagi, M.; Mamontov, E.; Pruski, M.; et al. Critical Role of Anion-Solvent Interactions for Dynamics of Solvent-in-Salt Solutions. *J. Phys. Chem. C* **2020**, *124* (16), 8457–8466. <https://doi.org/10.1021/acs.jpcc.9b10807>.
- (48) Wang, H.; Kim, S. C.; Rojas, T.; Zhu, Y.; Li, Y.; Ma, L.; Xu, K.; Ngo, A. T.; Cui, Y. Correlating Li-Ion Solvation Structures and Electrode Potential Temperature Coefficients. *J. Am. Chem. Soc.* **2021**, *143* (5), 2264–2271. <https://doi.org/10.1021/jacs.0c10587>.
- (49) Maryott, A. A.; Smith, E. R. *Table of Dielectric Constants of Pure Liquids*; Washington D.C., 1951.
- (50) Viti, V.; Zampetti, P. Dielectric Properties of 2-Methoxyethanol and 1,2-Dimethoxyethane: Comparison with Ethylene Glycol. *Chem. Phys.* **1973**, *2*, 233–238. [https://doi.org/10.1016/0301-0104\(73\)80009-6](https://doi.org/10.1016/0301-0104(73)80009-6).
- (51) Adams, B. D.; Zheng, J.; Ren, X.; Xu, W.; Zhang, J. G. Accurate Determination of Coulombic Efficiency for Lithium Metal Anodes and Lithium Metal Batteries. *Adv. Energy Mater.* **2018**, *8* (7), 1–11. <https://doi.org/10.1002/aenm.201702097>.
- (52) Rustomji, C. S.; Yang, Y.; Kim, T. K.; Mac, J.; Kim, Y. J.; Caldwell, E.; Chung, H.; Meng, Y. S. Liquefied

Gas Electrolytes for Electrochemical Energy Storage Devices. *Science* (80-. ). **2017**, *356* (6345).

<https://doi.org/10.1126/science.aal4263>.

- (53) Gao, Y.; Rojas, T.; Wang, K.; Liu, S.; Wang, D.; Chen, T.; Wang, H.; Ngo, A. T.; Wang, D. Low-Temperature and High-Rate-Charging Lithium Metal Batteries Enabled by an Electrochemically Active Monolayer-Regulated Interface. *Nat. Energy* **2020**, *5* (7), 534–542.  
<https://doi.org/10.1038/s41560-020-0640-7>.
- (54) Dong, X.; Lin, Y.; Li, P.; Ma, Y.; Huang, J.; Bin, D.; Wang, Y.; Qi, Y.; Xia, Y. High-Energy Rechargeable Metallic Lithium Battery at  $-70^{\circ}\text{C}$  Enabled by a Cosolvent Electrolyte. *Angew. Chemie - Int. Ed.* **2019**, *58* (17), 5623–5627. <https://doi.org/10.1002/anie.201900266>.
- (55) Stoltz, L.; Homann, G.; Winter, M.; Kasnatscheew, J. The Sand Equation and Its Enormous Practical Relevance for Solid-State Lithium Metal Batteries. *Mater. Today* **2021**, *44* (April), 9–14.  
<https://doi.org/10.1016/j.mattod.2020.11.025>.
- (56) Bai, P.; Li, J.; Brushett, F. R.; Bazant, M. Z. Transition of Lithium Growth Mechanisms in Liquid Electrolytes. *Energy Environ. Sci.* **2016**, *9* (10), 3221–3229. <https://doi.org/10.1039/c6ee01674j>.
- (57) Brissot, C.; Mosso, M.; Chazalviel, J.-N.; Lascaud, S. Dendritic Growth Mechanisms in Lithium/Polymer Cells. *J. Power Sources* **1999**, *81–82*, 925–929.
- (58) Cai, G.; Holoubek, J.; Li, M.; Gao, H.; Yin, Y.; Yu, S.; Liu, H.; Pascal, T. A.; Liu, P. Solvent Selection Criteria for Temperature-Resilient Lithium – Sulfur Batteries. **2022**, 1–9.  
<https://doi.org/10.1073/pnas.2200392119/-DCSupplemental.Published>.
- (59) Yamada, Y.; Chiang, C. H.; Sodeyama, K.; Wang, J.; Tateyama, Y.; Yamada, A. Corrosion Prevention Mechanism of Aluminum Metal in Superconcentrated Electrolytes. *ChemElectroChem* **2015**, *2* (11), 1687–1694. <https://doi.org/10.1002/celc.201500235>.

- (60) Cao, X.; Ren, X.; Zou, L.; Engelhard, M. H.; Huang, W.; Wang, H.; Matthews, B. E.; Lee, H.; Niu, C.; Arey, B. W.; et al. Monolithic Solid–Electrolyte Interphases Formed in Fluorinated Orthoformate-Based Electrolytes Minimize Li Depletion and Pulverization. *Nat. Energy* **2019**, *4* (9), 796–805. <https://doi.org/10.1038/s41560-019-0464-5>.
- (61) Xue, W.; Huang, M.; Li, Y.; Zhu, Y. G.; Gao, R.; Xiao, X.; Zhang, W.; Li, S.; Xu, G.; Yu, Y.; et al. Ultra-High-Voltage Ni-Rich Layered Cathodes in Practical Li Metal Batteries Enabled by a Sulfonamide-Based Electrolyte. *Nat. Energy* **2021**, *6* (5), 495–505. <https://doi.org/10.1038/s41560-021-00792-y>.
- (62) Zhang, E.; Chen, Y.; Yu, Z.; Cui, Y.; Bao, Z. Monofluorinated Ether Electrolyte with Acetal Backbone for High-Performance Lithium Metal Batteries. *Arxiv* **2023**.
- (63) Giffin, G. A. The Role of Concentration in Electrolyte Solutions for Non-Aqueous Lithium-Based Batteries. *Nat. Commun.* **2022**, *13*, 5250. <https://doi.org/10.1038/s41467-022-32794-z>.
- (64) Borodin, O.; Self, J.; Persson, K. A.; Wang, C.; Xu, K. Uncharted Waters: Super-Concentrated Electrolytes. *Joule* **2020**, *4* (1), 69–100. <https://doi.org/10.1016/j.joule.2019.12.007>.
- (65) Yamada, Y.; Wang, J.; Ko, S.; Watanabe, E.; Yamada, A. Advances and Issues in Developing Salt-Concentrated Battery Electrolytes. *Nat. Energy* **2019**, *4* (4), 269–280. <https://doi.org/10.1038/s41560-019-0336-z>.
- (66) Chen, Y.; Yu, Z.; Gong, H.; Zhang, W.; Rudnicki, P.; Huang, Z.; Yu, W.; Kim, S. C.; Boyle, D. T.; Sayavong, P.; et al. Failure Process During Fast Charging of Lithium Metal Batteries with 2 Weakly Solvating Fluoroether Electrolytes. *J. Phys. Chem. C* **2024**. <https://doi.org/10.1021/acs.jpcc.4c01740>.
- (67) Hoffman, Z. J.; Shah, D. B.; Balsara, N. P. Temperature and Concentration Dependence of the

Ionic Transport Properties of Poly ( Ethylene Oxide ) Electrolytes. *Solid State Ionics* **2021**, *370* (July), 115751. <https://doi.org/10.1016/j.ssi.2021.115751>.

- (68) Li, Y.; Li, Y.; Pei, A.; Yan, K.; Sun, Y.; Wu, C. L.; Joubert, L. M.; Chin, R.; Koh, A. L.; Yu, Y.; et al. Atomic Structure of Sensitive Battery Materials and Interfaces Revealed by Cryo-Electron Microscopy. *Science (80- ).* **2017**, *358* (6362), 506–510. <https://doi.org/10.1126/science.aam6014>.
- (69) Interphases, B. S.; Huang, W.; Wang, H.; Boyle, D. T.; Li, Y.; Cui, Y. Resolving Nanoscopic and Mesoscopic Heterogeneity of Fluorinated Species in Battery Solid-Electrolyte Interphases by Cryogenic Electron Microscopy. *ACS Energy Lett.* **2020**, *5*, 1128–1135. <https://doi.org/10.1021/acsenergylett.0c00194>.
- (70) Lee, C.; Yang, W.; Parr, R. G. Development of the Colle-Salvetti Correlation-Energy Formula into a Functional of the Electron Density. *Phys. Rev. B* **1988**, *37*, 785–789.
- (71) Grimme, S.; Antony, J.; Ehrlich, S.; Krieg, H. A Consistent and Accurate Ab Initio Parametrization of Density Functional Dispersion Correction (DFT-D) for the 94 Elements H-Pu. *J. Chem. Phys.* **2010**, *132*, 154104. <https://doi.org/10.1063/1.3382344>.
- (72) Grimme, S.; Ehrlich, S.; Goerigk, L. Effect of the Damping Function in Dispersion Corrected Density Functional Theory. *J. Comput. Chem.* **2011**, *32*, 1456–1465. <https://doi.org/10.1002/jcc>.
- (73) Weigend, F.; Ahlrichs, R. Balanced Basis Sets of Split Valence, Triple Zeta Valence and Quadruple Zeta Valence Quality for H to Rn: Design and Assessment of Accuracy. *Phys. Chem. Chem. Phys.* **2005**, *7*, 3297–3305. <https://doi.org/10.1039/b508541a>.
- (74) Neese, F.; Wennmohs, F.; Becker, U.; Ripplinger, C. The ORCA Quantum Chemistry Program Package. *J. Chem. Phys.* **2020**, *152*, 224108. <https://doi.org/10.1063/5.0004608>.

- (75) Abraham, M. J.; Murtola, T.; Schulz, R.; Páll, S.; Smith, J. C.; Hess, B.; Lindah, E. Gromacs: High Performance Molecular Simulations through Multi-Level Parallelism from Laptops to Supercomputers. *SoftwareX* **2015**, 1–2, 19–25. <https://doi.org/10.1016/j.softx.2015.06.001>.
- (76) Wang, J.; Wolf, R. M.; Caldwell, J. W.; Kollman, P. A.; Case, D. A. Development and Testing of a General Amber Force Field. *J. Comput. Chem.* **2004**, 25, 1157–1174. <https://doi.org/10.1002/jcc.20035>.
- (77) Sousa Da Silva, A. W.; Vranken, W. F. ACPYPE - AnteChamber PYthon Parser InterfacE. *BMC Res. Notes* **2012**, 5, 367. <https://doi.org/10.1186/1756-0500-5-367>.
- (78) Wang, J.; Wang, W.; Kollman, P. A.; Case, D. A. Automatic Atom Type and Bond Type Perception in Molecular Mechanical Calculations. *J. Mol. Graph. Model.* **2006**, 25, 247–260. <https://doi.org/10.1016/j.jmgm.2005.12.005>.
- (79) Frisch, M. J.; Trucks, G. W.; Schlegel, H. B.; Scuseria, G. E.; Robb, M. A.; Cheeseman, J. R.; Scalmani, G.; Barone, V.; Petersson, G. A.; Nakatsuji, H.; et al. Gaussian 16, Revision B.01. Gaussian Inc. Wallingford CT 2016.
- (80) Self, J.; Fong, K. D.; Persson, K. A. Transport in Superconcentrated LiPF<sub>6</sub> and LiBF<sub>4</sub>/Propylene Carbonate Electrolytes. *ACS Energy Lett.* **2019**, 4 (12), 2843–2849. <https://doi.org/10.1021/acsenergylett.9b02118>.
- (81) Michaud-Agrawal, N.; Denning, E. J.; Woolf, T. B.; Beckstein, O. Software News and Updates MDAnalysis: A Toolkit for the Analysis of Molecular Dynamics Simulations. *J. Comput. Chem.* **2011**, 32 (10), 2319–2327. <https://doi.org/10.1002/jcc.21787>.